

## Body-wave reconstruction from ambient seismic noise correlations in an underground mine

Gerrit Olivier<sup>1</sup>, Florent Brenguier<sup>2</sup>, Michel Campillo<sup>2</sup>, Richard Lynch<sup>3</sup>, and Philippe Roux<sup>2</sup>

### ABSTRACT

The reconstruction of seismic Green's functions from correlations of ambient seismic noise has recently developed as a promising approach for exploring the earth's interiors without the requirement of costly active seismic sources. This approach is widely used for imaging the crust at a kilometer scale. However, few studies report noise-based Green's function reconstruction at smaller scales in industrial environments. We have investigated the possibility of constructing seismic Green's functions between sensors in an active underground mine (Garpenberg, Sweden) by crosscorrelating seismic noise generated by mining activities. We have determined with realistic numerical simulations that the mining excavations in an underground mine lead to a regime of strong scattering, which is favorable for constructing seismic Green's functions by crosscorrelating seismic noise. One month of continuous data was recorded by 18 seismic sensors located

more than 1 km below surface. A variety of broadband (10–3000 Hz) seismic sources were present, but the seismic wavefields are directional and often monochromatic, so that the conditions for constructing Green's functions by crosscorrelating ambient seismic noise were not ideal (isotropic illumination and spectrally white). We developed a stacking scheme that dismissed data during periods when the seismic noise was dominated by monochromatic signals or when noise sources were not in stationary phase locations. Estimates of the seismic Green's functions were retrieved for a broad frequency range (20–400 Hz) for almost all of the correlation pairs when we used the selective stacking scheme. We used the direct body waves present at low frequencies (less than 100 Hz) in the reconstructed seismic Green's functions to invert for the 3D S-wave velocity structure of the mine. Our results revealed the existence of a high-velocity zone and a low-velocity zone that corresponded with known ore bodies.

### INTRODUCTION

Crosscorrelating ambient seismic noise can be used to construct the seismic Green's function between sensors pairs, effectively turning one of the sensors into a virtual source (Shapiro and Campillo, 2004; Sabra et al., 2005b; Campillo, 2006; Stehly et al., 2008).

Over the past decade, Green's functions, constructed by crosscorrelating ambient seismic noise, have been predominantly used to image the upper crustal structure of the earth (Sabra et al., 2005a; Shapiro et al., 2005; Moschetti et al., 2007; Lin et al., 2013a, 2013b; Boué et al., 2014). The vast majority of ambient noise tomography studies have been performed with surface waves because the sensor arrays used for these studies are located at the surface and the seismic

noise is dominated by the surface waves emanating from the interaction of the ocean with the solid earth (Webb, 1998). Constructing body waves by crosscorrelating ambient seismic noise has proven to be much more difficult (Forghani and Snieder, 2010), but there are a few notable examples in which body waves have been extracted from ambient seismic noise (Roux et al., 2005; Zhang et al., 2009; Nakata et al., 2011; Boué et al., 2013).

To construct full Green's functions between sensors by crosscorrelating seismic noise, sensors should be surrounded in all directions by a large (theoretically infinite) number of spectrally white sources (Lobkis and Weaver, 2001), or spectrally white sources should only be located in stationary phase locations (Roux and Kuperman, 2004).

Manuscript received by the Editor 29 June 2014; revised manuscript received 9 December 2014.

<sup>1</sup>Université Joseph Fourier, Institut des Sciences de la Terre, Grenoble, France and Institute of Mine Seismology, Kingston, Tasmania, Australia. E-mail: gerrit.olivier@imseismology.org.

<sup>2</sup>Université Joseph Fourier, Institut des Sciences de la Terre, Grenoble, France. E-mail: florent.brenguier@ujf-grenoble.fr; michel.campillo@ujf-grenoble.fr; philippe.roux@ujf-grenoble.fr.

<sup>3</sup>Institute of Mine Seismology, Kingston, Tasmania, Australia. E-mail: richard.lynch@imseismology.org.

© 2015 Society of Exploration Geophysicists. All rights reserved.

The stationary phase locations of a sensor pair refer to the conical areas behind each sensor pointing toward the other. An isotropic seismic wavefield and a directional seismic wavefield can produce the same crosscorrelation function (CCF); for isotropic wavefields, signals not coming from stationary phase locations destructively interfere so that only signals from sources located in stationary phase locations contribute to the CCF (Gouedard et al., 2008). This property is useful for small-scale and high-frequency applications in which local sources strongly contribute to the seismic wavefields so that the resulting seismic wavefields are not isotropic.

Currently, most mines with seismic monitoring networks only use a small fraction of the recorded vibrations, in the form of microseismic events, whereas all other data are discarded. Although a large number of these microseismic events are recorded in a given day, using them to examine the properties of the surrounding medium is difficult because the exact location and start time of these events are unknown. This means that prior information about the seismic velocities has to be used to determine the start time and location of the events. These same events are then used to try and iteratively improve the velocity models, which is somewhat ambiguous. Therefore, not knowing the exact start time and location of the source signals reduces the achievable accuracy of the final velocity model. Furthermore, there is no control over the location of the events so that the spatial resolution is dependent on the distribution of the microseismic events; we cannot perform tomographic inversion in areas in which no rays from microseismic events pass through. Here, the advantages of using ambient seismic noise to construct virtual source signals becomes apparent: We know the exact location (location of the sensors) and start time (zero lag time in correlation functions) of our virtual source signals so that the accuracy of the achievable velocity model is higher. We can also control the spatial resolution by installing sensors in locations where greater resolution is required and we use all the available data.

In this study, we investigate the possibility of constructing seismic Green's functions between sensors by crosscorrelating ambient noise recorded in an active underground mine. One month of continuous data recorded with the standard mine seismic monitoring network (<http://www.imseismology.org>) at Boliden's Garpenberg mine (Sweden) was examined.

In the first section of this article, we construct and use a 3D model of the mining excavations (tunnels, stopes, voids, caves, etc.) inside homogeneous host rock to generate numerical estimates of the seismic Green's functions between sensor pairs. We use these numerical Green's functions to approximate the scattering (caused by known mining excavations) of the seismic waves propagating between sensors to examine if these excavations create favorable conditions for reconstructing seismic Green's function by crosscorrelating ambient noise.

In the following section, we describe the different seismic noise sources that contribute to the recorded continuous data and examine the associated spectral properties. We find that the ambient seismic noise recorded in the underground mining environment is not ideal to construct seismic Green's functions between sensors by crosscorrelating ambient noise with conventional methods. Although sources of seismic energy were located in many different locations during the recording period, the noise is dominated by vibrations associated with mining activities, which are often peaked in frequency and not distributed evenly around the seismic sensors. In other words, seismic noise sources in an active underground mine

are not spectrally white and the seismic wavefield is not isotropic but directional.

In the final section, we show that the large number of noise sources and the strong scattering caused by mining excavations create similar conditions in which estimates of the Green's function can be retrieved, if CCFs are only considered when broadband noise sources are positioned, or scattered off excavations, in stationary phase locations. To identify time periods in which these conditions are reasonably met, we develop and implement a selective stacking algorithm.

For most of the station pairs, we retrieve convincing Green's functions in the frequency band 20–400 Hz after the selective stacking algorithm is implemented. Two different frequency bands are used for different applications. We pick the arrival times of the body waves to perform an inversion for the 3D velocity structure of the underground mine for frequencies less than 100 Hz, and we use the multiply scattered waves in the reconstructed Green's functions to determine the scattering properties of the seismic waves caused by the mining excavations at frequencies greater than 200 Hz.

## NUMERICAL SIMULATIONS

Seismic sources generated by industrial activity are not favorable for Green's function reconstruction because they are localized in space and peaked in frequency. However, the seismic waves are scattered and each scatterer can act as a secondary source when enough seismic energy is present to excite it. The combination of these primary and secondary sources could yield more isotropic illumination, which is favorable for Green's function reconstruction by crosscorrelating seismic noise. It is thus important to understand the scattering caused by known excavations in the studied medium. In this section, we use numerical simulations of seismic waves propagating between sensors to evaluate the scattering caused by mining excavations in the studied underground mine.

In many underground mines, the locations of the strong scatterers (mining excavations) are known to a good accuracy. Additionally, the average P- and S-wave velocities are known from calibration blasts. This gives an excellent opportunity to numerically calculate Green's functions between sensor pairs.

To numerically model seismic Green's functions between sensor pairs, we construct a 3D structural model of the mining excavations inside the host rock and use a finite-difference kinematic seismic wavefield modeling code to generate synthetic seismograms between sensors. Because we use an impulsive, spectrally white source to generate the synthetic seismograms, these seismograms can be considered as numerical Green's functions. With these numerical Green's functions, we examine the scattering of the seismic waves caused by the mining excavations by calculating the average distance the seismic waves travel before they scatter (mean free path). Because the mining excavations are the only heterogeneities included in the otherwise homogeneous numerical model, we can compare the mean free path calculated from the numerical Green's function and the mean free path calculated from actual seismic data to reveal if the mining excavations are predominantly responsible for the scattering of the seismic waves in an underground mining environment.

### Creating a realistic model

We construct the numerical model from the known mining excavations that are present at Boliden's Garpenberg mine in Sweden

(see Figure 1). In the numerical model, we model all the points inside tunnels as air points with  $V_s = 0$  m/s,  $V_p = 300$  m/s,  $\rho = 1$  g/m<sup>3</sup>, and near-zero  $Q$ -factor ( $Q = 0.01$ ). We construct the rest of the model as the host rock with  $V_p = 6650$  m/s,  $V_s = 3850$  m/s,  $\rho = 2700$  kg/m<sup>3</sup>, and frequency-dependent  $Q$ -factor  $Q(f) = 10 * Q_f/f$  with  $Q_f = 1000$  Hz. The P- and S-wave velocities we chose are close to the values used by the mine to locate seismic events and have been determined by five calibration blasts that were performed on 8 August 2012 ( $V_p = 6645 \pm 70$  m/s and  $V_s = 3828 \pm 85$  m/s), whereas the density is representative of the average density of the host rock and the  $Q$ -factor is chosen so that  $Q(100 \text{ Hz}) = 100$ . To eliminate reflections from the boundaries of the model, we use absorbing boundary layers below and alongside the model, with a reflecting surface at the top, which represents the surface of the earth.

The resulting model was roughly 4.2 km<sup>3</sup> in size ( $3.5 \times 1.7 \times 0.7$  km). With 2-m-grid spacing, this amounts to approximately 500 million grid points. The grid spacing here is dependent on the frequency content we want to consider. Because

signals of up to 400 Hz will be considered, the shortest wavelengths will be approximately 10 m. The rule of thumb with numerical simulations is that each wavelength has to be sampled by at least five samples, so at most, 2-m grid spacing is needed to adequately sample waves of all frequencies considered. Although the grid spacing is not small enough to sample the propagation of the acoustic waves through the air in the tunnels, we do not care about these acoustic waves but only the seismic waves scattered off the mining excavations.

Although the model contains realistic approximations of the mining excavations, it assumes that the excavations are surrounded by homogeneous host rock. Reality is somewhat more complicated: Excavations have a fracture zone surrounding them, and the host rock is inhomogeneous, especially close to surface where the host rock is layered. These inaccuracies make the multiply scattered coda part of Green's functions hard to model. The goal of generating the numerical Green's functions is, therefore, not to exactly retrieve the seismic Green's function, but rather to examine the scattering of the seismic waves by the known mining excavations so that

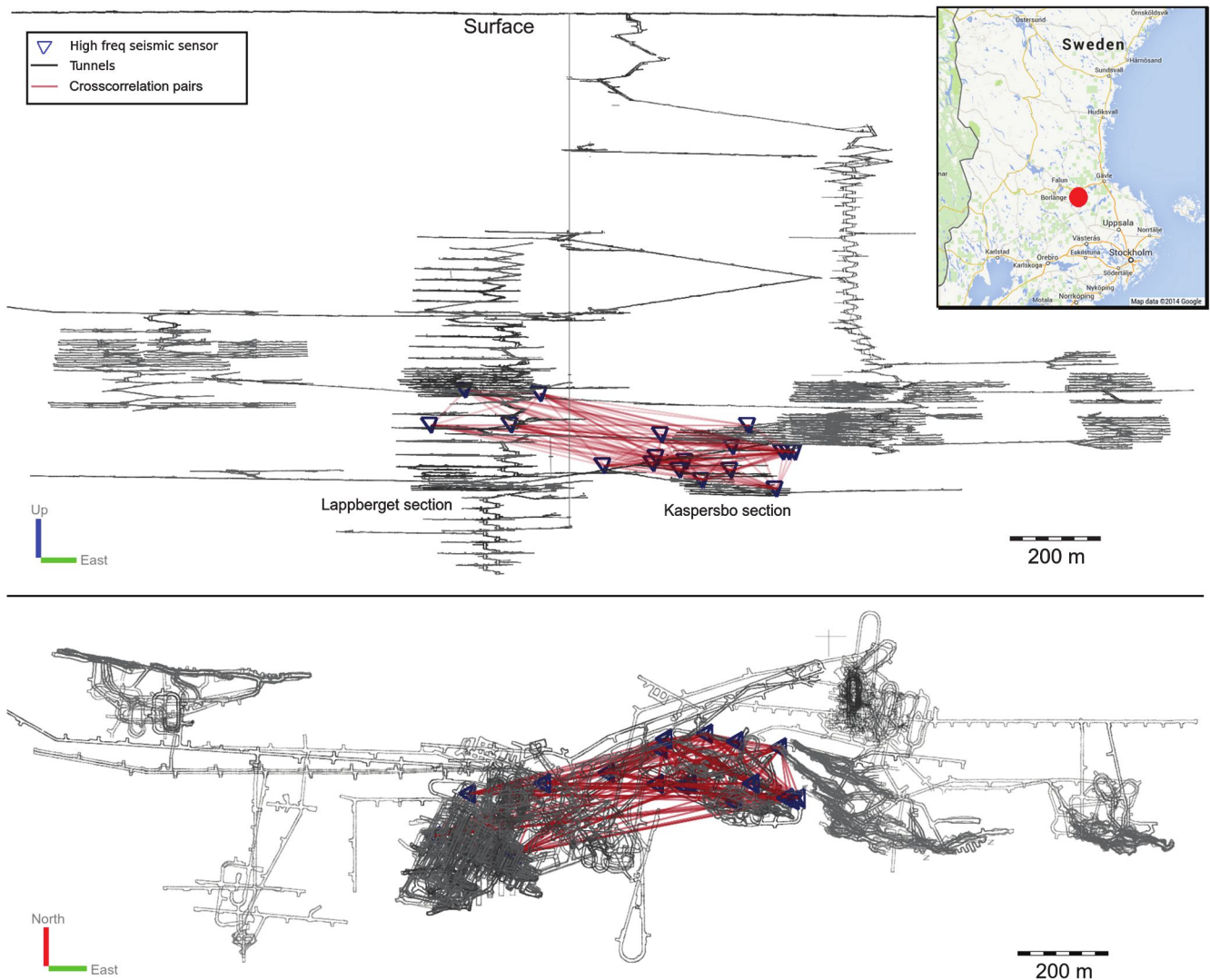


Figure 1. Section view and plan view of Boliden's Garpenberg mine in Sweden. The sensors are indicated by blue triangles, the raypaths of the crosscorrelation pairs are shown in red, and mining tunnels are in gray. The red dot in the inset shows the regional location of the mine.

we can determine if the excavations are the dominant cause of scattering of the seismic waves in the underground mining environment. If the mining excavations do cause significant scattering of the seismic waves propagating in the mining area, it could prove beneficial for reconstruction seismic Green's functions by crosscorrelating seismic noise in sensor pairs because these excavations would themselves act as secondary sources (Derode et al., 2003).

### Scattering caused by mining excavations

We want to investigate the influence of the mining excavations on the seismic waves propagating between sensors, to determine if the scattering caused by them are beneficial for constructing CCFs that resemble seismic Green's functions. To do this, we generate numerical Green's functions between all seismic sensors. In each simulation, we replace one of the 18 sensors with an impulsive, spectrally white source in a downward ( $-z$ ) direction and record the vertical ground motion ( $z$ ) traces on the other sensors. We create the source by applying a band-pass filter in the frequency range 20–400 Hz to an impulsive signal. We choose this frequency range to compare the results with the ambient noise crosscorrelations later in this article.

In Figure 2, we show a comparison of the seismograms of a source-receiver pair 400 m apart, in which the tunnels and excavations were included and excluded in the numerical model. The inclusion of the tunnels dramatically changes the shape of the recorded seismograms in three ways: (1) the coda part of the wave-

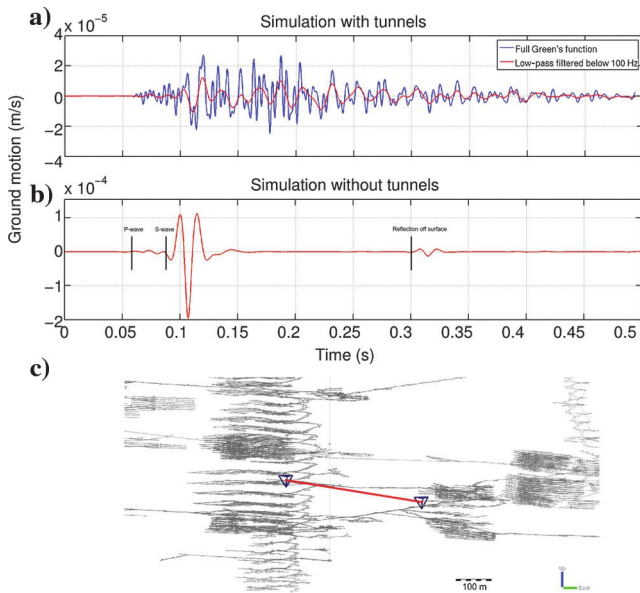


Figure 2. The difference between synthetic seismograms with and without the tunnels and excavations included in the model but with the same source time function (impulsive downward). When tunnels and excavations are included in the model, the seismic waves scatter multiple times and a lot of energy is present in the coda part of the seismogram. For the synthetic seismogram recorded when the tunnels are not included, the only remarkable feature after the body-wave arrivals (weak P-wave and strong S-wave) is the reflection off the free surface at roughly 0.31 s. When the tunnels are included, the direct S-wave arrival is only visible for lower frequencies (less than 100 Hz) and the reflection off the free surface is buried by the multiply scattered waves in the coda.

form is extended due to the scattering caused by excavations, (2) when the tunnels are included, a clear direct S-wave arrival is only visible in the low-frequency part (less than 100 Hz) of the seismogram, and (3) the highest amplitude is observed after the direct wave arrivals.

When strong multiple scattering occurs, it has been shown that the amplitude of the coda waves can be larger than the direct arrivals (Nakamura, 1977). For multiply scattered waves, we can model seismograms with the diffusion model when the time is larger than the average time the seismic waves travel before scattering (mean free time) (Wegler and Luhr, 2001). By transforming seismograms to energy density and comparing them with different energy densities that are modeled by the diffusion model, we can isolate the energy loss due to scattering and intrinsic attenuation (see the details in Appendix A). When we construct the numerical model, we explicitly specify the intrinsic attenuation ( $Q$ -factor); therefore, when modeling the numerical seismograms with the diffusion model, the only parameter to fit is the scattering attenuation coefficient  $\eta_s$ . The mean free path is given by the inverse of the scattering attenuation coefficient  $\eta_s^{-1}$ .

In Figure 3, we show the process of transforming a seismogram to the energy density and inverting for the mean free path with the diffusion model. The details of this inversion are given in Appendix A. The average value of the mean free path for the 153 station pairs was found to be 33 m with a standard deviation of 9 m. The minimum value was 16 m, and the maximum value was 56 m. In general, the mean free path was found to be slightly higher in the Lappberget section than in the Kaspersbo section (see Figure 1).

The diffusion model is a very simplified model that assumes strong scattering. The conditions necessary for strong scattering to occur and the diffusion model to be reasonable are that the wavelength of the seismic waves should be much smaller than the mean free path and the distance between the source and receiver. The mean free path we find in Figure 3 is 32 m for the frequency range 170–220 Hz. This length is roughly the same as the wavelength of an S-wave of frequency 120 Hz. Therefore, for the rest of the article, we will only attempt to calculate the mean free path for frequencies greater than 200 Hz. For frequencies greater than 200 Hz, we also ensure that the distance between the source and receiver is much larger than the wavelengths of the seismic waves for almost all station pairs.

### Influence of source-receiver distance on scattering regime

The level of diffraction of the seismic signal is related to the ratio of the source-receiver distance to the mean free path. If the distance between the source and receiver is much larger than the average distance before the seismic wave scatters, multiply scattered waves arrive at the receiver shortly after the primary waves (Margerin et al., 2000). This scenario is referred to as the *multiply scattered regime*. However, if the distance between source and receiver is less than the average distance before the seismic wave scatters, this is not the case and the waves are in the single-scatter regime.

The signatures of the single-scatter regime are clear direct arrivals and short coda waves indicating little scattering. For the numerical simulations, we find that the waves are in the single-scatter regime for lower frequencies because clear direct arrivals are visible. For higher frequencies, the direct arrivals are not clearly visible and the coda parts of the waveforms are extended; in this case, the signals

are in the multiply scattered regime. Although the frequencies in which the different scattering regimes occur are different for each source-receiver pair, we generally find that for frequencies of less than 100 Hz, the waves are in the single-scatter regime and for frequencies of greater than 200 Hz, the waves are in the multiply scattered regime (see Figures 5 and 11).

The fact that for frequencies less than 100 Hz, the waves propagating between sensors are in the single scatter regime does not mean that the low-frequency seismic waves in the ambient noise are not scattered by the mining excavations before they are recorded by the seismic sensors. Rather, the seismic sensors are too close to each other for the longer wavelengths going from one sensor to the other to be multiply scattered.

Throughout this article, we use the two scattering regimes for two different applications: For frequencies of less than 100 Hz (the single-scatter regime), we identify the direct arrivals and use them with tomographic inversion to determine the local velocity structure, whereas for frequencies of greater than 200 Hz (the multiply scattered regime), we fit the diffusion model to the waves and determine the mean free path of the medium.

## DATA

The seismic monitoring network consists of seven triaxial and 11 uniaxial short-period 14-Hz geophones. The geophones were permanently installed into boreholes 10 m above tunnel structures. Signals were sampled at 6000 samples per second, and time synchronization is achieved over dedicated fiber-optic cables from the central GPS receiver to each of the underground stations. The intersensor distances range between 13 and 900 m, and the sensors are located roughly 1 km below surface. In Figure 1, we show the mine plans with the location of the seismic sensors relative to the mining excavations. At this depth, the sensors are not in the layered host rock close to the surface and far enough above the tunnels to be out of the zone of fractured rock surrounding them (estimated by the mine to be 5 m). This is advantageous when looking at high-frequency content that is normally attenuated very quickly close to the surface (Frankel et al., 1990; Picozzi et al., 2009).

In Figure 4, we show an example of 5 s of continuous seismogram data. The first part of the seismogram shows the repetitive signal resulting from impacts of a hammer drill that was roughly 120 m away from the sensor. Drilling, which will typically occur in many places simultaneously, is very energetic and has broad spectral content that is beneficial for reconstructing a seismic Green's function if drilling occurs in stationary phase locations. The second part of the signal has no noteworthy attributes and consists of noise generated by multiple sources far away, such as air vents and trucks. Although the strength of this section of noise is low compared to the first section, the level is still an order of magnitude above the electronic self-noise level of the analog/digital converter. The power spectral density of this part shows that mechanical sources are very peaked in frequency. The third part of the signal shows a microseismic event. This event has a local magnitude of  $-3$  and was located roughly

30 m away from the seismic sensor. The data slice shows that the sources of seismic signal can change in a short period of time. The drilling in this example changes the amplitude of the background seismic signal multiple orders of magnitude in a matter of seconds. The power spectral density of each of the three parts shows that during the second part of the signal, the noise is dominated by monochromatic sources.

## Examining scattering properties with microseismic events

To examine how realistic the mean free paths obtained from the numerical simulations are, we consider microseismic events recorded and located by the seismic monitoring network during June 2013. In Figure 5, we show one of these microseismic events in two different frequency bands. In the low-frequency band (less than 100 Hz), the direct P- and S-wave arrivals are visible (indicated on the figure), whereas in the high-frequency band (greater than 200 Hz), the arrivals are not clear. We can confirm that these arrivals are P- and S-waves by (1) determining the traveltime residual of the direct arrivals after the event is located by the seismic monitoring system and (2) by the ratio of the apparent P-wave velocity over the S-wave velocity of the direct arrivals. If the traveltime residual is small, and the  $V_P/V_S$  ratio is close to  $\sqrt{3}$ , the arrivals are confirmed to be P- and S-waves.

In Figure 5, we show the inversion for the mean free path for frequencies greater than 200 Hz (see Appendix A for details). The value of the mean free path we found by the inversion is 43 m. This value is close to the value found with the numerical simulations. Because we only include mining excavations inside the homogeneous host rock in the numerical model and we obtain similar values for the mean free path with actual seismic data, it confirms that the mining excavations are the dominant cause of scattering in an underground mining environment.

By filtering the seismogram in different frequency bands, we show the possibility of using the same signal for different applica-

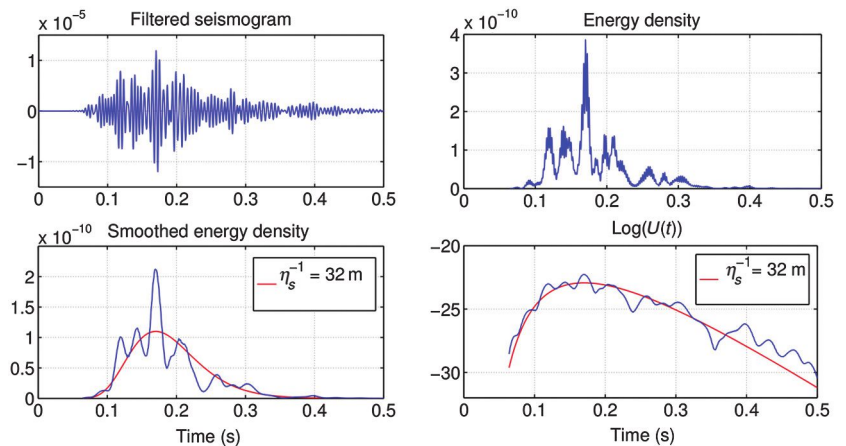


Figure 3. The processing steps taken to invert for the mean free path with the synthetic seismograms. Panel (a) shows the seismogram band-pass filtered in the range 170–220 Hz. Panel (c) shows the seismogram after it has been transformed to energy density defined in equation A-3. Panel (b) shows the energy density after it was smoothed by a 100-ms box window with the control curve (inversion result) in red. Panel (d) shows the logarithmic function from equation A-2 along with the computed inversion result in red. The mean free path that fits the synthetic data the best was found to be 32 m for this frequency range.

tions. The low-frequency content of the seismic waves displays direct body-wave arrivals; we pick these arrivals and use it to establish a velocity model of the medium. The high-frequency content does not show clear body-wave arrivals because the wavefield is diffuse; we use this part to approximate the scattering properties (such as the mean free path) of the medium.

From the dramatic change in the waveforms after the tunnels were inserted in the numerical model and the low mean free path obtained from the inversion of synthetic and real data at high frequency, it is clear that the tunnels and excavations cause the seismic waves to be highly scattered before they are recorded by the seismic sensors. This scattering ensures that high-frequency signals are in the multiple scattering regime even when the source-receiver distance is as low as 100 m, which will prove to be beneficial when we are constructing CCFs. If we can construct good

estimates of Green's functions by crosscorrelating ambient seismic noise, we can examine the material properties of the surrounding medium with greater accuracy than by using microseismic events.

### AMBIENT NOISE CROSSCORRELATIONS

In general, it is assumed that the longer the duration of the seismic signal used to construct CCFs, the better the convergence of the correlation function to the Green's function will be due to the reduction of random fluctuations and the enhanced contribution of weak sources (Larose et al., 2008). In this section, we explore an optimized way of retrieving Green's functions in the conditions of nonstationary industrial sources of seismic noise.

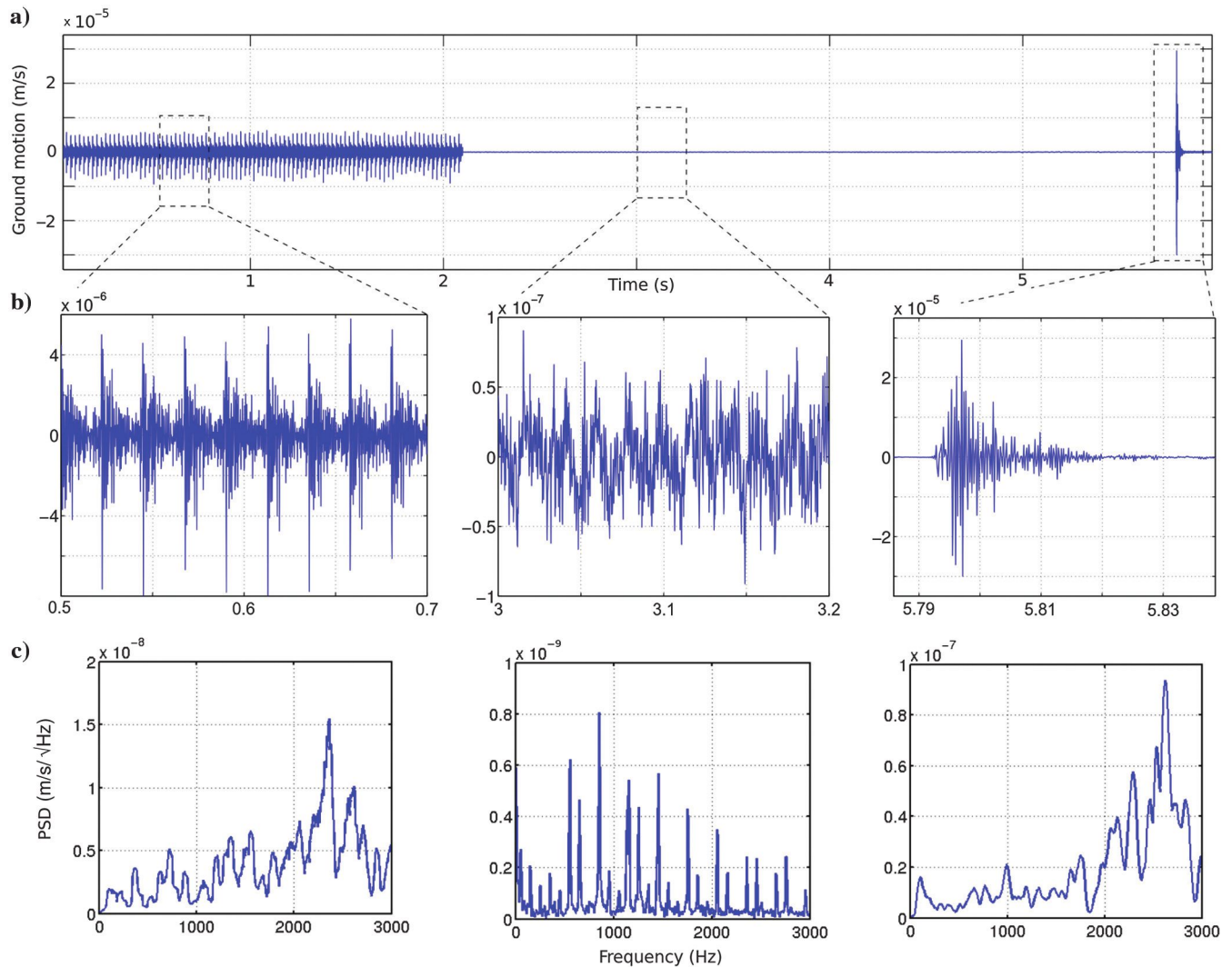


Figure 4. A seismicogram of length 5 s showing the changes in seismic noise. Three distinct time periods have been marked in the seismicogram: In the first block, the repetitive impacts of a hammer drill is visible. Drilling occurs in multiple places during a normal day of mining. The second block shows no distinct features. The noise here is due to a combination of far-away sources such as trucks, ventilation fans, and ore crushing. In the third block, a recorded microseismic event is shown. This event has a local magnitude of  $-3$  and was located roughly 30 m away from the seismic sensor. Thousands of these microseismic events happen in a given day. The bottom three windows show the power spectral density of each time period. For the middle time period with background noise, it is clear that the signal is very peaked in frequency, whereas for the other two periods, seismic energy is present in a broad frequency range from 10 to 3000 Hz.

## Stationary phase locations

The seismic Green's functions can be reconstructed by crosscorrelating spectrally white seismic noise coming from all exterior directions recorded in two sensors (Lobkis and Weaver, 2001) or by crosscorrelating spectrally white noise only coming from stationary phase locations (Roux and Kuperman, 2004). In an active underground mine, the seismic noise is dominated by local mining activities so that the resulting seismic wavefields are directional. When crosscorrelating directional seismic wavefields, only station pairs that are favorably aligned so that the noise is propagating in the stationary phase directions will succeed in recovering the seismic Green's functions.

Because of the noisy nature of an underground mine, it is reasonable to assume after an adequate amount of time that there are noise sources located at almost every location in the mining excavations. (All excavations should at least experience traffic from underground vehicles at some point in a one-month period.) Additionally, the mining excavations could scatter incoming seismic waves and, therefore, themselves act as secondary seismic sources when enough seismic energy is present to excite them (Derode et al., 2003). Although the seismic wavefields are directional and the mining excavations are not spatially distributed all around the seismic sensors, when we consider Figure 1, it seems likely that many of the sensor pairs could at some point have seismic energy propagating from (or scattered off) their corresponding stationary phase locations.

## Monochromatic sources

In general, mechanical sources (pumps, fans, etc.) are expected to be peaked in frequency. When monochromatic sources dominate the noise records, the CCF will have regularly spaced peaks in which the lag time between peaks corresponds to the monochromatic phase. When we blindly use all data recorded for this study to construct correlation functions, the correlation functions have peaks at regular intervals, which shows that it is dominated by monochromatic sources or sources that are peaked in frequency (Figure 4b).

We determine that these regularly spaced peaks in the correlation functions are due to ventilation fans in the tunnels, which are very strong, stable sources that are peaked in frequency. These fans are so stable that whitening the signals before crosscorrelating is not sufficient to suppress them. If we stack enough of the individual CCFs, the regularly spaced peaks reappear due to their stability and strength. This phenomenon can be seen in Figure 6, in which we show that selectively stacking a subset of one month of data yields a more convincing estimate of the Green's function than stacking all the data. We discuss the selective scheme used to determine the subset of data in the following section.

The abundant sources, together with the strong scattering properties established earlier, indicate that theoretical conditions exist for creating good estimates of the seismic Green's functions by crosscorrelating ambient noise for station pairs that are favorably orientated. The challenge is to only use the sources in stationary phase loca-

tions to create the correlation functions and to dismiss the data from strong, stable monochromatic sources or sources in nonstationary phase locations.

## Selective stacking

To dismiss data from monochromatic sources and sources in nonstationary phase locations, we develop a selective stacking scheme. This scheme identifies time periods when noise sources are located in stationary phase locations (and are not monochromatic), and it only uses correlation functions during these times to add to the stacks for individual station pairs.

To identify the periods when the noise is coming from stationary phase locations, we calculate the rms of the signal in the lag-time window of the correlation function around the expected arrival times of the S-waves and divide it by the rms of the signal in the far coda part of the signal to get an effective S/N. The lag-time window we consider for calculating the S/N is the distance between sensors divided by the S-wave velocity  $\pm 30\%$  ( $[d/0.7 \times V_S, d/1.3 \times V_S]$ ). This lag-time window is wide enough to ensure that sufficient individual time periods pass the stacking criteria so that the stacked correlation functions converge to stable waveforms.

If we only stack the CCFs when the S/N is high in the expected arrival time window, it increases the chances of selecting time periods in which the noise sources are located in or scattered off the stationary phase locations. For sources in nonstationary phase locations (that do not scatter off mining excavations in stationary phase locations), the correlation functions will have a peak at earlier lag times and no peaks in the expected arrival time window. Selective stacking also dismisses time periods in which the noise is dominated by monochromatic sources or sources in nonstationary phase locations. In the presence of monochromatic sources, the correlation functions have a low S/N because of the regularly spaced peaks.

We spectrally whiten short continuous data slices (10 s) between 20 and 400 Hz for each seismic sensor and crosscorrelate them to construct individual CCFs. Although a lot of seismic energy is

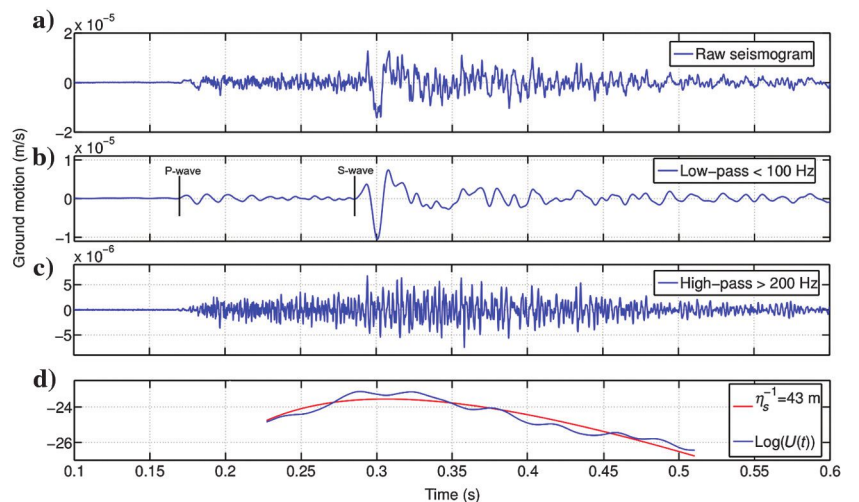


Figure 5. A recorded microseismic event filtered in the low-frequency band (less than 100 Hz) and the high-frequency band (greater than 200 Hz). In the low-frequency band, the direct P- and S-wave arrivals are picked, and in the high-frequency band, the mean free path is determined (see Appendix A). The mean free path found by the inversion here is 43 m. The low value of the mean free path for the microseismic event is in agreement with the numerical simulations performed in the ‘‘Introduction’’.

present at higher frequencies (see Figure 4), we find that the frequency window maximizes the S/N of the final CCFs. Also, as shown in the previous section, the higher frequency content is not useful for tomography because the waves are in the multiply scattered regime. Because the nature of the noise can change rapidly in a

matter of seconds (see Figure 4), it is important that we only consider 10-s intervals at a time, because a longer period could contain a mix of short seismic signals in stationary phase locations and monochromatic sources or sources that are not located in stationary phase locations. We did not perform time-domain normalization (one-bit normalization) to try to preserve the dominant influence of energetic seismic signals (such as microseismic events, drilling, blasting, etc.) in stationary phase locations. If the S/N of an individual CCF for a station pair is higher than 4, the individual CCF is weighted by the square of the S/N and added to the total stack for the station pair. By weighting the CCFs, we favor the time periods when energetic seismic sources are in stationary phase locations in the stack. For some station pairs, we find that the weighting of the correlation functions is enough to suppress the monochromatic signal, but for most of the station pairs (with one or more sensors close to a ventilation fan) that this is not the case and the selection criterion is necessary.

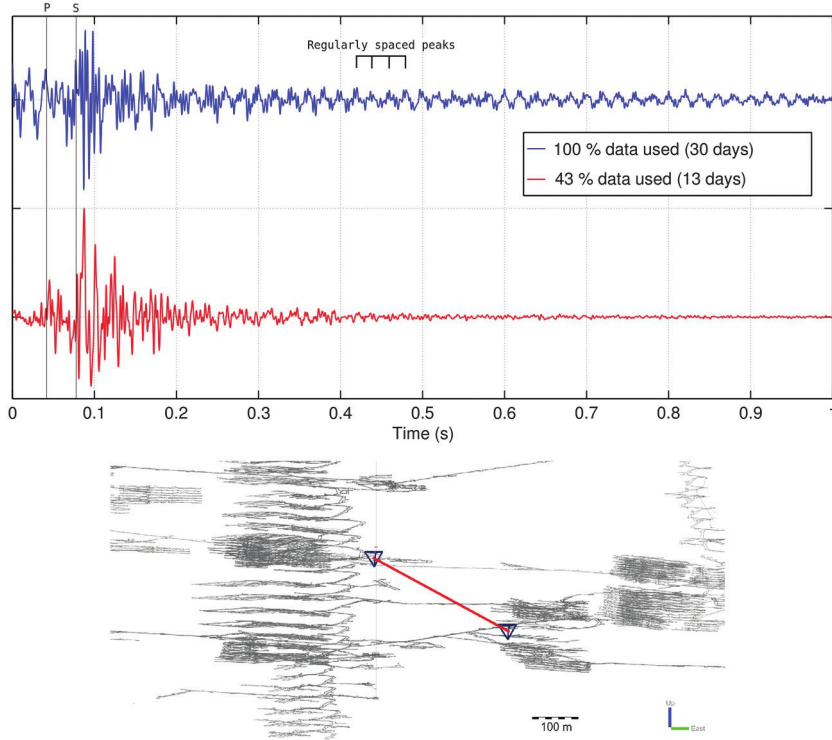


Figure 6. Comparison of the CCF for one station pair when a subset of 43% of the data is stacked compared to the (b) CCF when (a) all of the data are stacked. The CCF shows direct P- and S-wave arrivals when 43% of the data is used. The expected P- and S-wave arrivals are indicated by black lines. The direct arrivals are not clearly visible when all the data are used. Instead, we see regularly spaced peaks because of the influence of monochromatic sources.

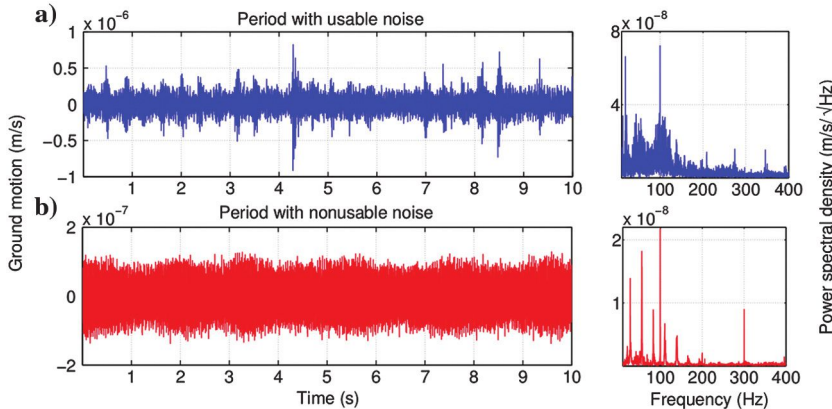


Figure 7. Two 10-s periods of continuous data recorded by the same sensor at different times. (a) 61% of the correlation pairs passed the selective stacking criteria. This is thanks to the multiple sources and broadband content of the data. In panel (b), only 13% of the correlation pairs passed the selective stacking criteria. During this time, the noise is dominated by ventilation fans that are very peaked in frequency.

In Figure 7, we show 10-s intervals of continuous data recorded by the same sensor at different times. In Figure 7a, the noise is usable for many station pairs because multiple sources are present and seismic energy is contained in a broad frequency band. During this time, 61% of the correlation pairs pass the selective stacking criterion. For the time period shown in Figure 7b, the magnitude of the seismic noise is significantly less and the noise is dominated by monochromatic signals from the ventilation fans. During this time period, only 13% of the correlation functions pass the stacking criterion due to the monochromatic nature of the seismic noise recorded in most of the sensors.

In Figure 8, we compare the results of conventional blind vertical stacking and selective stacking for all 153 ZZ-components of the correlation functions between sensor pairs. For Figure 8a in which we use blind vertical stacking, no clear wave arrival fronts can be seen. For Figure 8b, in which we use the selective stacking, an arrival front is visible at positive and negative lag times. The velocity of the arrival front is close to the current S-wave velocity used with the monitoring network to locate microseismic events (3828 m/s), even though the selection window is wide. For the 3C sensors that were available, we examine the polarity of these waves to confirm that they are in fact S-waves. The S/N of the S-wave arrivals is significantly increased by using the amplitude selective stacking scheme. In Figure 8c, we show the ZZ-component of the numerical Green's functions generated in the "Introduction" section. The ZZ-components of the numerical Green's functions show a weak P-wave arrival front and a strong S-wave arrival front (indicated by black lines).

The ZZ-components of the CCFs do not show a clear P-wave arrival front. For some CCFs, an apparent P-wave arrival is visible (see Figures 6, 10, and 11), but most CCFs do not. This is contrary to the idea that anthropogenic noise (drilling, hammers, etc.) consists mostly of P-wave energy, but we argue that there are three main reasons why the S-wave arrival front is more clearly visible than a P-wave arrival front: (1) The ZZ-component CCFs represent the signal recorded on the Z-component of one sensor if the other sensors was an impulsive source in the  $z$ -direction. Because the sensors are roughly on the same horizontal plane, we therefore expect the S-waves to be the strongest. The ZZ-components of the numerical Green's tensor in Figure 8 show a weak P-wave arrival front and a stronger S-wave arrival front, which confirms this observation. (2) The selective stacking scheme selects periods when the  $S/N$  of the correlation functions in the lag-time window corresponding to the expected S-wave arrival time is high; therefore, with the stacking scheme, we explicitly select times when the noise consists of S-waves. We purposefully choose the lag-time window around the expected S-wave arrival time window because it is hard to determine if the seismic energy in the lag-time window corresponding to the expected P-wave arrival time consists of P-waves in stationary phase locations or of S-waves in nonstationary phase locations. (3) It is known that multiply scattered waves consist mostly of S-waves because P-waves are converted to S-waves more frequently than vice versa (Aki, 1992), so that continuous data are expected to consist mostly of multiply scattered S-waves, regardless of the source.

### Directional bias from nonisotropic wavefields

Because sources of seismic signals (and mining excavations that act as secondary sources) are not uniformly distributed around our monitoring network, a directional bias is possible in the CCFs that could influence the tomography results (Tsai, 2009; Weaver et al., 2009). The potential error in the apparent velocity is inversely proportionate to the interstation distance, so that sensor pairs close to each other are more likely to be affected. Furthermore because we choose the time window for the selective stacking scheme to be wide ( $V_S \pm 30\%$ ), if there are constant strong noise sources that dominate the stack of CCFs, the error in apparent velocity can be up to 30%. To reduce the potential errors in the final tomography result, we could either narrow the window of the selective stacking scheme and/or we could only consider pairs far apart. If we narrow the window, we greatly reduce the amount of data used and artificially constrain the velocity to the expected value. Also, because most of the sensors are less than 200 m apart, the achievable resolution of the model decreases significantly if we only consider sensors further apart. Instead, we only consider sensors further than 100 m apart, and we only accept S-wave picks that are within 10% of the expected S-wave velocity (see Appendix B). This results in 121 of the 153 crosscorrelation pairs to be usable in the tomography.

Apart from phase shifts, the causal (positive lag time) and acausal (negative lag time) could have different amplitudes depending on how frequently sources are located in each corresponding stationary phase location. This is confirmed in Figure 9, in which we show a sensor pair in which many mining excavations are located in the stationary phase location of signals going from sensor A to sensor B, but there are not many excavations for signals going from B to A. Accordingly, the CCF has a strong apparent S-wave arrival in the causal part (the signal from A to B) and a comparatively weak

S-wave in the acausal part (the signal from B to A) present in the CCF.

### Convergence of CCFs to the seismic Green's functions

In Figure 10, we show the convergence of a CCF to a stable function after a sufficient amount of data has been processed. In this case, after roughly 12 h of raw time (8h effective time), a strong S-wave arrival is visible. When we correlate and stack more data, the amplitude of nonphysical arrivals (around zero lag time) is decreased, and finally, after processing one month of raw continuous

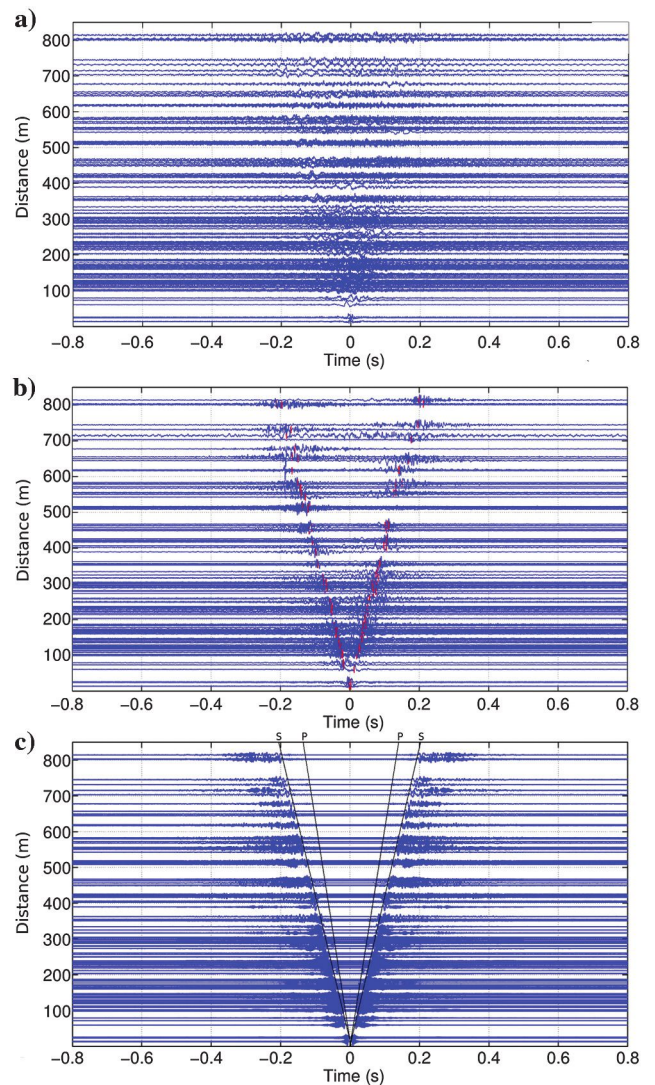


Figure 8. CCFs arranged by the intersensor distance. Panel (a) shows the CCFs when conventional blind vertical stacking is applied. No clear arrival fronts are visible. Panel (b) shows the CCFs when the selective stacking scheme is applied. An S-wave arrival front is visible. The picks that were obtained by the kurtosis-based algorithm are shown in red. Panel (c) shows the synthetic Green's functions generated with numerical simulations. The synthetic Green's functions show a weak P-wave arrival and a strong S-wave arrival. The expected arrival times in the synthetic Green's functions are shown with black lines.

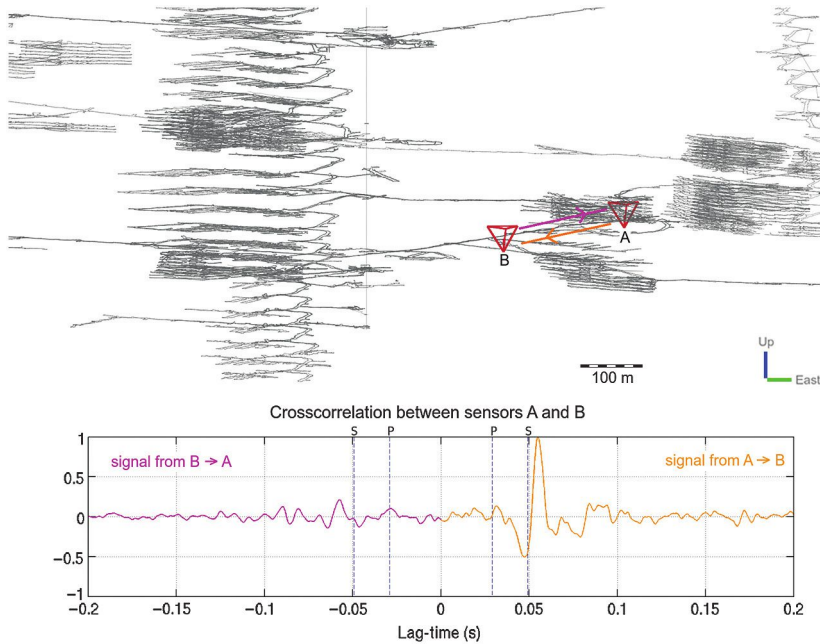


Figure 9. The location of two sensors and the crosscorrelation of the seismic noise recorded in them when the selective stacking scheme is used. The causal part (orange) of the CCF has a strong apparent S-wave arrival, whereas the acausal part (purple) has a comparatively weak S-wave arrival. The directional bias of the CCF can be described by the scatterers in the stationary phase locations: Behind sensor A, there are many mining excavations that ensure that seismic waves propagate from the stationary phase location from A to B regularly, whereas behind sensor B, there are not as many mining excavations so that seismic waves do not propagate from the stationary phase location from B to A as frequently.

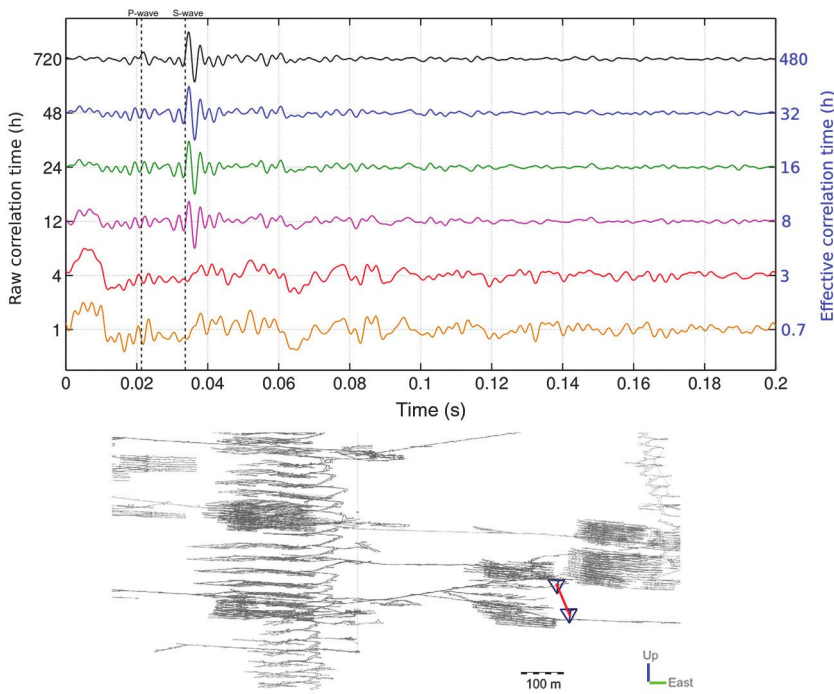


Figure 10. The convergence of the CCF to Green's function. The S-wave arrival is stable after 12 h (8 h effective time). After 30 days (20 days effective time), the nonphysical arrivals are weaker and a faint P-wave arrival can be seen. The effective time refers to cumulative time that passed the selective stacking criteria, and therefore, the actual amount of data is used to construct the correlation functions.

data (20 days effective time), a weak P-wave arrival is visible. In general, we find that the rate of convergence of the CCF to Green's function is dependent on the intersensor distance, with the pairs closer together converging faster than the pairs further apart, as expected. Additionally, the larger the intersensor distance, the more energetic sources are needed to satisfy the selective stacking criteria. This means that the percentage of data used to construct the CCFs is inversely proportional to the intersensor distance.

### Frequency content of the crosscorrelation functions

Because we find that seismic Green's functions can be constructed for a broad frequency range (20–400 Hz), we can use different frequency bands for different applications (as discussed in the previous section). In Figure 11, we show a CCF split in two frequency bands. Below 100 Hz, direct P- and S-waves arrivals can be seen (indicated in the figure), whereas above 200 Hz, this is not the case. This is because above 200 Hz, the wavefield is diffuse due to the scattering caused by the mining excavations. Figure 11b shows the result of the inversion we obtain for the mean free path when the CCF is high-pass filtered above 200 Hz. The average value of the mean free path calculated for all 153 CCFs was found to be 39 m with a standard deviation of 17 m; this observation is consistent with the results from the numerical simulations and microseismic data. In the following section, we use the lower frequency content of the CCFs to invert for the local velocity structures by picking the arrival times of the direct S-waves.

### 3D S-wave velocity model

Most underground mines use an isotropic homogeneous seismic velocity model in routine microseismic monitoring. The average velocities are determined by calibration blasts or minimizing the traveltimes residual for a large number of events recorded by multiple sensors (Mendecki and Sciocatti, 1997). This simple velocity model is predominantly used because of the relatively small errors in seismic event locations and also because of the difficulty of conducting the many calibration blasts required to calibrate a full 3D velocity model. An accurate 3D inhomogeneous velocity model would improve the location accuracy of seismic events and could also indicate geologic features near the mine.

The details of the automatic picking of the S-wave arrivals and the inversion process are given in Appendix B. We show the successful picks of the CCFs with intersensor distance larger than 100 m in Figure 12. The traveltimes misfit of the S-wave picks for the homogeneous model with

least-squares solution of  $V_S = 3862$  m/s is 3.2 ms. The traveltime misfit for the final result of the inversion is 2.5 ms. This corresponds to a misfit reduction of 22%.

We show the final result of the velocity inversion in Figure 13. The 3D S-wave velocity model shows a high S-wave velocity zone in the Kaspersbo section (on the right) and a low S-wave velocity structure in the Lappberget section (on the left). These two sections consist of two known ore bodies. The locations of these ore bodies are shown by wire frames determined by drill samples in the bottom of Figure 13. The location of the ore body in the Kaspersbo section is in agreement with the high-velocity zone from the inversion, but the low-velocity zone is mispositioned with regard to the Lappberget ore body. This is because most of the Lappberget ore body is outside the grid where we invert for the velocity. According to geologists at Garpenberg, the ore body in Kaspersbo has significantly different material properties to the ore body in Lappberget — Most notably, there are many silica and skarn intrusions in Kaspersbo. The silica and skarn intrusions simultaneously decrease the average density and increase the shear modulus of the bulk medium as observed in laboratory measurements on core samples (Boliden, 2014). A decrease in density and an increase in shear modulus are expected to increase the S-wave velocity of the medium (Aki and Richards, 2002).

An alternative explanation for the higher and lower S-wave velocity found in the Kaspersbo and Lappberget sections could be the uneven distribution of noise sources because it has been shown that nonisotropically distributed noise sources can lead to errors in the apparent arrival times in CCFs as discussed earlier. The error in traveltimes for direct arrivals induced by nonisotropically distributed wave intensities has been studied with theoretical methods (Froment et al., 2010) and with field data (Yao and van der Hilst, 2009) and in both cases was found to be negligible (less than 1%) for tomographic studies. Therefore, we consider that the different

material properties are the true explanation for the apparent high- and low-velocity structures in the final S-wave velocity model.

## CONCLUSIONS

In this article, we have investigated the possibility of using seismic sensors installed at depth along with seismic noise generated by mining activities to estimate the seismic Green’s functions between sensors. The results of numerical simulations indicated that seismic waves are highly scattered by mining excavations, indicated by the

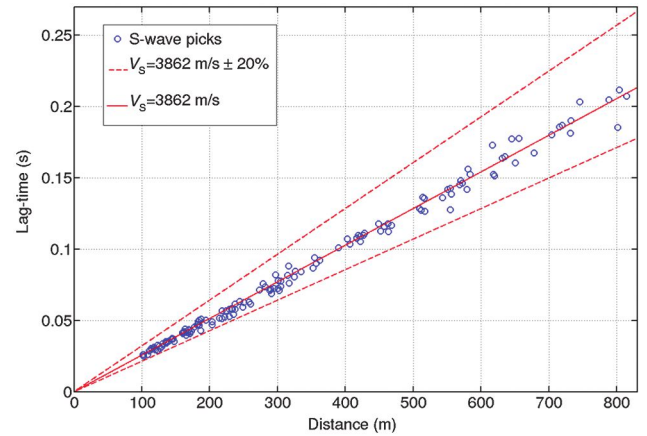


Figure 12. The S-wave picks (blue) from the automatic kurtosis-based algorithm along with the homogeneous least-squares solution (solid red) as a function of distance for CCFs with successful S-wave picks. The maximum allowed picking variations are indicated by the red dashed lines. The picking constraints ensure that other local maxima (scattered P- or S-waves) are not mistakenly picked as S-wave arrivals.

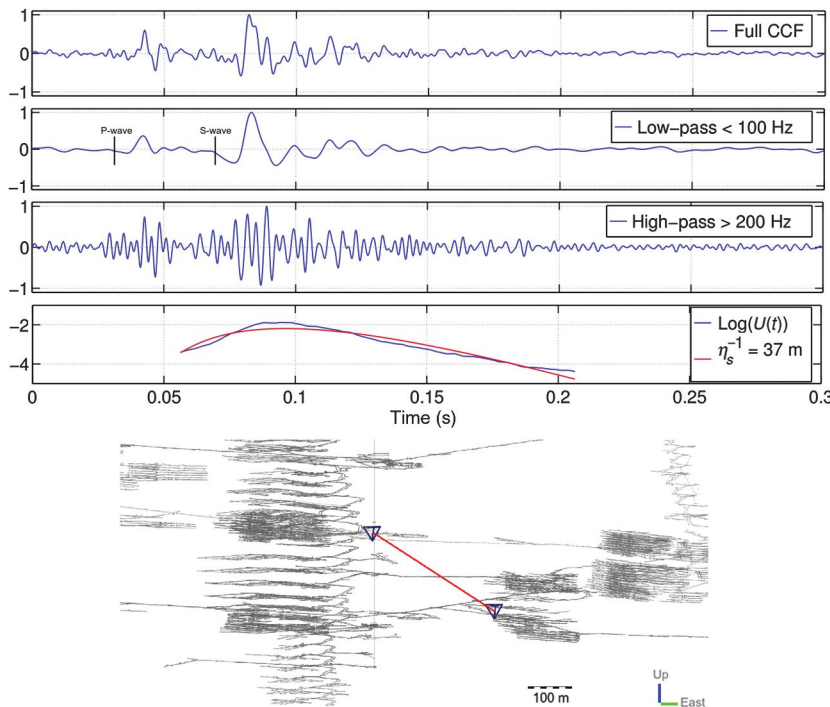


Figure 11. The different frequency components of the CCF. Direct P- and S-wave arrivals are visible for the low-frequency part of the CCF, whereas the high-frequency part is diffuse due to the scattering by the tunnels and excavations. As a result, there are no clear direct P- and S-wave arrivals. The inversion of the mean free path is shown in the bottom window and was determined to be 37 m.

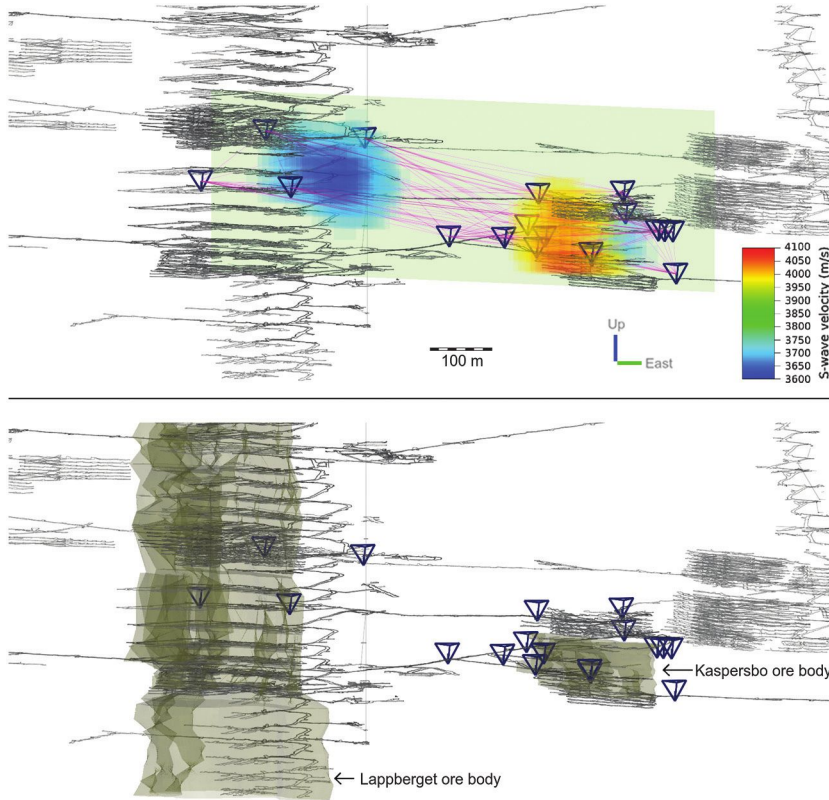


Figure 13. The 2D cross section of the result of the 3D S-wave velocity inversion. The velocity is slightly higher in the tunnel network in the Kaspersbo section on the right and slightly lower in the tunnel network in the Lappberget section on the left. The outlines of known ore bodies are shown in the bottom figure. The locations of these ore bodies are determined by drill samples. The high-velocity structure overlaps with the Kaspersbo ore body.

average distance the waves travel before they are scattered (mean free path) that we found was roughly 35 m by modeling the numerical seismograms with the diffusion model in the frequency band (170–220 Hz).

By inspecting the continuous data, we found that a large number of noise sources with broad frequency content are present in an active mine. Not all seismic waves generated by mining activities are useful to construct seismic Green's functions between sensors; more specifically stable, monochromatic vibrations from ventilation fans and sources in nonstationary phase locations dominate some CCFs, and they retard convergence to the seismic Green's functions. We have developed a selective stacking scheme that identifies time periods when sources were located in stationary phase locations (and not monochromatic) and that would, therefore, contribute positively toward reconstruction of the seismic Green's functions. This stacking scheme, along with the highly scattering medium, enabled us to retrieve estimates of the seismic Green's functions between sensors.

After we identified and used periods of time in which noise sources are in stationary phase locations (and not monochromatic), the CCFs showed direct S-wave arrivals and, in the case of favorable orientation, weak P-wave arrivals for low-frequency bands (lower than 100 Hz). We used the strong S-wave arrivals that are present for most of the crosscorrelation pairs at low frequencies to perform

an inversion for the 3D S-wave velocity structure of the area enclosed by the sensors. The 3D S-wave velocity structure shows the existence of a high-velocity zone and a low-velocity zone that correspond to known ore bodies with different material properties.

We used the higher frequencies contained in the CCFs (greater than 200 Hz) to determine the average distance the seismic waves travel before they are scattered (mean free path). We found the value of the mean free path with the CCFs to be approximately 37 m. This value compares well with the mean free path we found with numerical simulations when only mining excavations were included in the otherwise homogeneous model. This indicates that the mining excavations are predominantly responsible for the scattering in this environment.

The methodology we used in this study not only shows many potential applications in an underground mining environment, but also in any setting in which sensors are installed at depth and broadband seismic noise is locally generated. Other potential applications include imaging and monitoring oil and gas reservoirs, hydraulic fracturing wells, CO<sub>2</sub> sequestration reservoirs, geothermal reservoirs, and active fault zones with downhole sensors.

## ACKNOWLEDGMENTS

We would like to thank Boliden's Garpenberg mine in Sweden for giving permission to use the mine plans and data; the IMS research patrons for funding the project; N. Shapiro for the useful discussions; the Centre for High Performance Computing in Cape Town, South Africa, for giving access to computing facilities to run simulations and process data; and J. van der Neut, N. Nakata, and two anonymous reviewers for useful suggestions and comments.

## APPENDIX A

### INVERSION OF THE MEAN FREE PATH

As shown in (Dainty and Toksoz, 1981), the diffusion model describes the seismic energy for body waves as a function of space and time as

$$W(r, t) = E_0 \left( \frac{4\pi V_S t}{3\eta_s} \right)^{-3/2} \exp \left[ -\eta_i V_S t - \frac{3r^2 \eta_s}{4V_S t} \right], \quad (\text{A-1})$$

where  $E_0$  is the source energy,  $V_S$  is the S-wave velocity,  $r$  is the distance, and  $\eta_i$  and  $\eta_s$  are the coefficients for intrinsic and scattering attenuation, respectively. By choosing a reference distance,  $r_1$ , so that  $W_1(r_1, t_1) = 1 \text{ J m}^{-3}$  for  $t_1 = 1 \text{ s}$  in the same way as Wegler and Luhr (2001) do, we can linearize the diffusion model as

$$\ln U(t) = a_1 + a_2 t + a_3 \frac{1}{t}; \quad (\text{A-2})$$

here,  $U(t) = \frac{W(r,t)}{W_1} \left(\frac{t}{t_1}\right)^{3/2}$ ,  $a_1 = \ln \left[ \frac{E_0}{W_1} \left(\frac{4\pi V_s t_1}{3\eta_s}\right)^{-3/2} \right]$ ,  $a_2 = -\eta_i V_s$ , and  $a_3 = -3r^2 \eta_s / 4V_s$ .

To use the linearized form of the diffusion model and to determine the scattering coefficients for different frequencies, we filter seismograms in different frequency bands and transform from ground motion to energy density  $W(r, t)$  by

$$W(r, t) = \sum_{i=1}^3 [f_i(r, t)]^2 + [H\{f_i(r, t)\}]^2, \quad (\text{A-3})$$

where  $H\{f\}$  is the Hilbert transform of  $f$ , and  $f_i(r, t)$  is the filtered  $i$ -component seismogram at location  $r$  at time  $t$ . By now multiplying the energy density by the geometric factor  $t^{3/2}$  and taking the logarithm on both sides, we see that we construct the left side of equation A-2, which is only linearly dependent on the three base functions 1,  $t$ , and  $1/t$ . We can now perform a simple least-squares inversion to fit the linear function with the parameters  $a_1$ ,  $a_2$ , and  $a_3$  to the energy density. Because we know the S-wave velocity to a good degree, we can calculate the coefficients for intrinsic  $\eta_i$  and scattering attenuation  $\eta_s$  from  $a_2$  and  $a_3$ , respectively.

When we are considering synthetic data, the uncertainty of the result of the scattering attenuation coefficient is reduced by the fact that the inversion is performed for two variables  $a_1$  and  $a_3$  because the intrinsic attenuation is a specified value in our numerical model  $\eta_i = 10/V_s t_1$ . When using the microseismic data or the CCFs, in which the intrinsic attenuation is unknown, our inversion is identical to that used by [Wegler and Luhr \(2001\)](#).

## APPENDIX B

### DETERMINATION OF S-WAVE ARRIVAL WITH KURTOSIS ESTIMATOR

To construct a 3D S-wave velocity model from the source-receiver functions constructed by crosscorrelating ambient seismic noise, we determine the arrival times of these waves in the source-receiver functions. So, we use the commonly used method of constructing kurtosis estimators of the source-receiver functions ([Langet et al., 2014](#)). The standard definition of the kurtosis  $K$  of a signal  $x$  is given by

$$K(x_1, \dots, x_n) = \frac{1}{n} \sum_{j=1}^n \left[ \frac{x_j - \bar{x}}{\sigma} \right]^4, \quad (\text{B-1})$$

where  $\bar{x}$  is the mean of  $x$ , and  $\sigma$  is the standard deviation of  $x$ . As discussed by [Langet et al. \(2014\)](#), the maximum value of the kurtosis will be delayed in terms of the true first arrival. To reduce the bias (the delayed maximum of the kurtosis), we consider the arrival of the seismic wave to be the maximum of the positive time derivative of  $K$ , defined as  $dK_+ = dK/dt$  if  $dK/dt \geq 0$  or  $dK_+ = 0$  if  $dK/dt < 0$ . In Figure B-1, we show the result of the kurtosis estimator on one of the CCFs. The maximum of the kurtosis gradient is still slightly delayed with respect to the S-wave arrival. To reduce this delay, we use the Akaike information criteria (AIC) as defined by [Zhang et al. \(2003\)](#) in a window around the peak of the maximum of the kurtosis gradient and locate the minimum of the AIC. As explained in ([Zhang et al., 2003](#)), this gives a better estimate of the exact S-wave arrival time.

The automatic picking and detection of seismic waves is difficult for a number of reasons (for example, see the ‘‘Introduction’’ section of [Langet et al. \[2014\]](#)). For our study, it is much simpler because

we know the S-wave velocity, start time, and position of the virtual sources to a good degree. In other words, we only need to search for the S-wave arrivals in a small time window.

### 3D tomography

To invert for the 3D velocity model, we divide the area enclosing all source-receiver pairs into blocks. The size of these blocks will determine the resolution of our 3D velocity model. The volume enclosing the sensors is divided into blocks of  $8000 \text{ m}^3$  ( $20 \times 20 \times 20 \text{ m}$ ). When picking the arrival times of the S-waves, we consider waves of frequency between 20 and 100 Hz. S-waves with frequency of 100 Hz have a wavelength of roughly 40 m. Bearing this in mind, we spatially smooth the final velocity model in 3D with 40-m smoothing windows because smaller structures cannot be resolved with these wavelengths.

To ensure that the arrival times of the S-waves can accurately be picked, the intersensor distance needs to be larger than the wavelengths of the S-waves so that signals are not in the near field. For S-waves of 100 Hz, the wavelengths are roughly 40 m. Bearing this in mind, sensor pairs with an intersensor distance of more than 100 m were used to invert for the S-wave velocity model. Of the 153 crosscorrelation pairs, 144 had intersensor distances larger than 100 m. Of these 144 possible S-wave arrivals, 121 S-waves were successfully picked by the kurtosis estimator. For the 23 pairs that didn't have successful picks, the peak of the kurtosis estimator was less than a predefined threshold.

To obtain realistic results, the solution is constrained to a certain range. Because large deviations in the S-wave velocity are not expected at these depths, the solution is constrained to the range ( $0.8 \times v_s$  and  $1.2 \times v_s$ ). In Figure 12, we can see that the S-wave picks that were obtained by the kurtosis estimator fall comfortably inside this constraint. If the constraint is eased, some of the S-wave picks fall outside the 20% range and cause random scatter in the final velocity model. This indicates that if the constraint is too wide, the kurtosis estimator could mistake other local maxima in the CCF as the S-wave arrivals. The value of 20% was chosen because it resulted in a large reduction in traveltime misfit (22%), while not causing random scatter in the final velocity model.

An important point to note here is that straight rays are assumed between sensors. Although this assumption is incorrect, it is reasonable in this case for two reasons: First, the velocity variations are

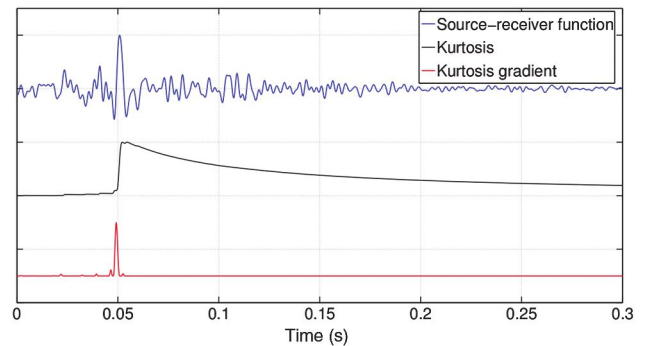


Figure B-1. Determining the S-wave arrival by the kurtosis estimator. We consider maximum value of the positive derivative of the kurtosis estimator as the arrival of the S-wave.

expected to be small in magnitude for the bulk medium. Second, the areas in which the velocity contrasts are high, such as the mining excavations, are spatially small enough so that the low-frequency components of the direct arrivals in the estimates of the seismic Green's functions will not be affected by them (see Figures 2, 5, and 11). To test if this assumption is valid, a numerical checkerboard velocity model is constructed. Synthetic Green's functions between sensors are generated with full-waveform modeling (see the "Numerical modeling" section), the arrival times of the S-waves are picked, and 3D inversion is performed to see if the input velocity model can be recovered. If the correct model is recovered, it will show that the straight-ray assumption is reasonable in this case. Although we made no direct estimates of the picking error, if the synthetic test reasonably recovers the checkerboard velocity model, we can also assume that the picking error is negligible for current purposes.

### Checkerboard resolution test

To assess the achievable resolution of the S-wave velocity inversion, we introduce blocks of consecutive high- and low-velocity

zones in our velocity model, construct synthetic Green's functions with numerical simulations, pick the arrival times of the synthetic S-waves, and finally attempt to retrieve blocks of high- and low-velocity zones. All the steps used in this synthetic test mimic the steps described in the manuscript for the CCFs.

The difference between the velocity model obtained by the inversion and the actual synthetic checkerboard velocity model used to generate the seismograms indicates the areas in which the achievable resolution is poor. It also indicates if the straight-ray assumption is reasonable and if the S-wave picking algorithm is accurate. The blocks were chosen to be  $3.4 \times 10^6 \text{ m}^3$  ( $150 \times 150 \times 150 \text{ m}$ ), and the variations used were 10% higher and lower than the background S-wave velocity, as shown in Figure B-2. These parameters were chosen bearing in mind the maximum velocity excursion we are expecting from the real data and the intersensor distance.

To do a realistic resolution test, only the 121 source-receiver functions for which we could find accurate S-wave picks in CCFs with real data are considered. The results of the checkerboard inversion are shown in Figure B-3. Almost all of the high- and low-velocity zones are recovered except for the section between the Kaspersbo and Lappberget ore bodies, which was to be expected due to the limited ray orientations of this section.

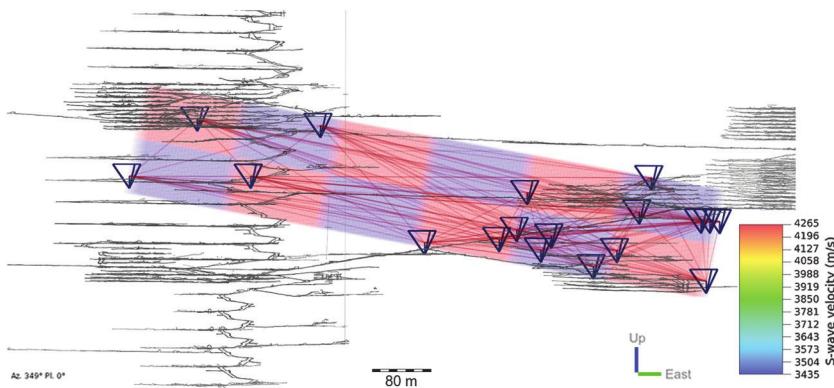


Figure B-2. The 2D cross section of the synthetic 3D velocity model used to create Green's functions for the checkerboard resolution test.

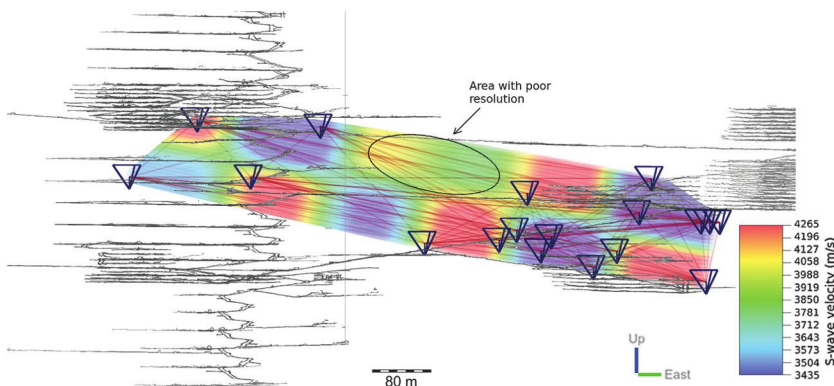


Figure B-3. The 2D cross section of the result from the inversion of data generated by the synthetic checkerboard velocity model. This shows the achievable resolution with the number of successful picks made of the S-wave arrivals of the CCFs. The outer edges of the checkerboard model cannot be retrieved because no rays pass through them. For the interior of the array, the correct velocities structures were mostly recovered.

### REFERENCES

- Aki, K., 1992, Scattering conversions P to S versus S to P: *Bulletin of the Seismological Society of America*, **82**, 1969–1972.
- Aki, K., and P. Richards, 2002, *Quantitative seismology*: University Science Books.
- Boliden, 2014, Laboratory measurements on core samples at Garpenberg: Internal communication.
- Boué, P., P. Poli, M. Campillo, H. Pedersen, X. Briand, and P. Roux, 2013, Teleseismic correlations of ambient seismic noise for deep global imaging of the earth: *Geophysical Journal International*, **194**, 844–848, doi: [10.1093/gji/ggt160](https://doi.org/10.1093/gji/ggt160).
- Boué, P., P. Poli, P. Roux, M. Campillo, and X. Briand, 2014, Phase velocity tomography of surface waves using ambient noise cross-correlation and array processing: *Journal of Geophysical Research*, **119**, 519–529, doi: [10.1002/2013JB010446](https://doi.org/10.1002/2013JB010446).
- Campillo, M., 2006, Phase and correlation in random seismic fields and the reconstruction of the Green Function: *Pure and Applied Geophysics*, **163**, 475–502, doi: [10.1007/s00024-005-0032-8](https://doi.org/10.1007/s00024-005-0032-8).
- Dainty, A., and M. Toksoz, 1981, Seismic codas on the earth and the moon: A comparison: *Physics of the Earth and Planetary Interiors*, **26**, 250–260, doi: [10.1016/0031-9201\(81\)90029-7](https://doi.org/10.1016/0031-9201(81)90029-7).
- Derode, A., E. Larose, M. Campillo, and M. Fink, 2003, How to estimate the Green's function for a heterogeneous medium between two passive sensors?: Application to acoustic waves: *Applied Physics Letters*, **83**, 3054–3056, doi: [10.1063/1.1617373](https://doi.org/10.1063/1.1617373).
- Forghani, F., and R. Snieder, 2010, Underestimation of body waves and feasibility of surface wave reconstruction by seismic interferometry: *The Leading Edge*, **29**, 790–794, doi: [10.1190/1.3462779](https://doi.org/10.1190/1.3462779).
- Frankel, A., A. McGarr, J. Bicknell, J. Mori, L. Seeber, and E. Cranswick, 1990, Attenuation of high-frequency shear waves in the crust: Measurements from New York State, South Africa, and southern California: *Journal of Geophysical Research, Solid Earth*, **95**, 17441–17457, doi: [10.1029/JB095iB11p17441](https://doi.org/10.1029/JB095iB11p17441).
- Froment, B., M. Campillo, P. Roux, P. Gouedard, A. Verdel, and R. Weaver, 2010, Estimation of the effect of non-isotropically distributed energy on the apparent arrival time in correlations: *Geophysics*, **75**, no. 5, SA85–SA93, doi: [10.1190/1.3483102](https://doi.org/10.1190/1.3483102).
- Gouedard, P., L. Stehly, F. Brenguier, M. Campillo, Y. C. de Verdiere, E. Larose, L. Margerin, P. Roux, F.

- Sanchez-Sesma, N. M. Shapiro, and R. Weaver, 2008, Cross-correlation of random fields: Mathematical approach and applications: *Geophysical Prospecting*, **56**, 375–393, doi: [10.1111/j.1365-2478.2007.00684.x](https://doi.org/10.1111/j.1365-2478.2007.00684.x).
- Langet, N., A. Maggi, A. Michelini, and F. Brenguier, 2014, Continuous kurtosis-based migration for seismic event detection and location, with application to Piton de la Fournaise Volcano, La Reunion: *Bulletin of the Seismological Society of America*, **104**, 229–246, doi: [10.1785/0120130107](https://doi.org/10.1785/0120130107).
- Larose, E., P. Roux, M. Campillo, and A. Derode, 2008, Fluctuations of correlations and Green's function reconstruction: Role of scattering: *Journal of Applied Physics*, **103**, 114907, doi: [10.1063/1.2939267](https://doi.org/10.1063/1.2939267).
- Lin, F., D. Li, R. W. Clayton, and D. Hollis, 2013a, High-resolution 3D shallow crustal structure in Long Beach, California: Application of ambient noise tomography on a dense seismic array: *Geophysics*, **78**, no. 4, Q45–Q56, doi: [10.1190/geo2012-0453.1](https://doi.org/10.1190/geo2012-0453.1).
- Lin, F., B. Schmandt, and V. Tsai, 2013b, Joint inversion of Rayleigh wave phase velocity and ellipticity using USArray: Constraining velocity and density structure in the upper crust: *Geophysical Research Letters*, **39**, 12303, doi: [10.1029/2012GL052196](https://doi.org/10.1029/2012GL052196).
- Lobkis, O., and R. Weaver, 2001, On the emergence of the Green's function in the correlation of a diffuse field: *Journal of the Acoustical Society of America*, **110**, 311–317, doi: [10.1121/1.1417528](https://doi.org/10.1121/1.1417528).
- Margerin, L., M. Campillo, and B. V. Tiggelen, 2000, Monte Carlo simulation of multiple scattering of elastic waves: *Journal of Geophysical Research*, **105**, 7873–7892, doi: [10.1029/1999JB900359](https://doi.org/10.1029/1999JB900359).
- Mendecki, A., and M. Sciocatti, 1997, *Seismic monitoring in mines*: Chapman and Hall.
- Moschetti, M. P., M. H. Ritzwoller, and N. Shapiro, 2007, Surface wave tomography of the western United States from ambient seismic noise: Rayleigh wave group velocity maps: *Geochemistry, Geophysics, Geosystems*, **8**, Q08010, doi: [10.1029/2007GC001655](https://doi.org/10.1029/2007GC001655).
- Nakamura, Y., 1977, Seismic energy transmission in an intensively scattering medium: *Journal of Geophysics*, **43**, 389–399.
- Nakata, N., R. Snieder, T. Tsuji, K. Larner, and T. Matsuoka, 2011, Shear wave imaging from traffic noise using seismic interferometry by cross-coherence: *Geophysics*, **76**, no. 6, SA97–SA106, doi: [10.1190/geo2010-0188.1](https://doi.org/10.1190/geo2010-0188.1).
- Picozzi, M., S. Parolai, D. Bindi, and A. Strollo, 2009, Characterization of shallow geology by high-frequency seismic noise tomography: *Geophysical Journal International*, **176**, 164–174, doi: [10.1111/j.1365-246X.2008.03966.x](https://doi.org/10.1111/j.1365-246X.2008.03966.x).
- Roux, P., and W. Kuperman, 2004, Extracting coherent wavefronts from acoustic ambient noise in the ocean: *Journal of the Acoustical Society of America*, **116**, 1995–2003, doi: [10.1121/1.1797754](https://doi.org/10.1121/1.1797754).
- Roux, P., K. Sabra, P. Gerstoft, and W. Kuperman, 2005, P-waves from crosscorrelation of seismic noise: *Geophysical Research Letters*, **32**, L19303, doi: [10.1029/2005GL023803](https://doi.org/10.1029/2005GL023803).
- Sabra, K., P. Gerstoft, P. Roux, W. Kuperman, and M. Fehler, 2005a, Surface wave tomography from microseisms in southern California: *Geophysical Research Letters*, **32**, L14311, doi: [10.1029/2005GL023155](https://doi.org/10.1029/2005GL023155).
- Sabra, K., P. Roux, and W. Kuperman, 2005b, Emergence rate of the time-domain Greens function from the ambient noise cross-correlation function: *Journal of the Acoustical Society of America*, **118**, 3524–3531, doi: [10.1121/1.2109059](https://doi.org/10.1121/1.2109059).
- Shapiro, N., M. Campillo, L. Stehly, and M. Ritzwoller, 2005, High resolution surface-wave tomography from ambient seismic noise: *Science*, **307**, 1615–1618, doi: [10.1126/science.1108339](https://doi.org/10.1126/science.1108339).
- Shapiro, N. M., and M. Campillo, 2004, Emergence of broadband Rayleigh waves from correlations of the ambient seismic noise: *Geophysical Research Letters*, **31**, L07614, doi: [10.1029/2004GL019491](https://doi.org/10.1029/2004GL019491).
- Stehly, L., M. Campillo, B. Froment, and R. Weaver, 2008, Reconstructing Green's function by correlation of the coda of the correlation ( $C^3$ ) of ambient seismic noise: *Journal of Geophysical Research*, **113**, B11306, doi: [10.1029/2008JB005693](https://doi.org/10.1029/2008JB005693).
- Tsai, V., 2009, On establishing the accuracy of noise tomography travel-time measurements in a realistic medium: *Geophysical Journal International*, **178**, 1555–1564, doi: [10.1111/j.1365-246X.2009.04239.x](https://doi.org/10.1111/j.1365-246X.2009.04239.x).
- Weaver, R., B. Froment, and M. Campillo, 2009, On the correlation of non-isotropically distributed ballistic scalar diffuse waves: *Journal of the Acoustical Society of America*, **126**, 1817–1826, doi: [10.1121/1.3203359](https://doi.org/10.1121/1.3203359).
- Webb, S., 1998, Broadband seismology and noise under the ocean: *Reviews of Geophysics*, **36**, 105–142, doi: [10.1029/97RG02287](https://doi.org/10.1029/97RG02287).
- Wegler, U., and B. Luhr, 2001, Scattering behaviour at Merapi volcano (Java) revealed from an active seismic experiment: *Geophysical Journal International*, **145**, 579–592, doi: [10.1046/j.1365-246x.2001.01390.x](https://doi.org/10.1046/j.1365-246x.2001.01390.x).
- Yao, H., and R. van der Hilst, 2009, Analysis of ambient noise energy distribution and phase velocity bias in ambient noise tomography, with application to SE Tibet: *Geophysical Journal International*, **179**, 1113–1132, doi: [10.1111/j.1365-246X.2009.04329.x](https://doi.org/10.1111/j.1365-246X.2009.04329.x).
- Zhang, H., C. Thurber, and C. Rowe, 2003, Automatic P-wave arrival detection and picking with multiscale wavelet analysis for single-component recordings: *Bulletin of the Seismological Society of America*, **93**, 1904–1912, doi: [10.1785/0120020241](https://doi.org/10.1785/0120020241).
- Zhang, J., P. Gerstoft, and P. Shearer, 2009, High-frequency P-wave seismic noise driven by ocean winds: *Geophysical Research Letters*, **36**, L09392, doi: [10.1029/2009GL037761](https://doi.org/10.1029/2009GL037761).